processes

MDPI

Article

Optimal Magnetic Graphite Heater Design for Impurity Control in Single-Crystal Si Grower Using Crystal Growth Simulation

Hye Jun Jeon [1,2,†], Hyeonwook Park [1,†], Salh Alhammadi [1], Jae Hak Jung [1,*] and Woo Kyoung Kim [1,*]

[1] School of Chemical Engineering, Yeungnam University, Gyeongsan 38541, Korea; daivjeon@ynu.ac.kr (H.J.J.); greatekal@naver.com (H.P.); salehalhammadi.1987@gmail.com (S.A.)
[2] R&D Team, S-TECH Co., Ltd., Daegu 42921, Korea
* Correspondence: jhjung@ynu.ac.kr (J.H.J.); wkim@ynu.ac.kr (W.K.K.); Tel.: +82-53-810-2514 (W.K.K.)
† These authors contributed equally to this work.

Abstract: In this paper, we report a successfully modified single-crystal Si growth furnace for impurity control. Four types of arbitrary magnetic heater (AMGH) systems with 3, 4, 5, and poly parts were designed in a coil shape and analyzed using crystal growth simulation. The concentration of oxygen impurities in single-crystal Si ingots was compared among the designed AMGHs and a normal graphite heater (NGH). The designed AMGHs were confirmed to be able to control turbulence and convection in a molten state, which created a vortex that influenced the oxygen direction near the melt–crystal interface. It was confirmed that replacing NGH with AMGHs resulted in a reduction in the average oxygen concentration at the Si melt–crystal interface by approximately 4.8%.

Keywords: single crystal silicon; arbitrary magnetic device; impurity; graphite heater; crystal growth furnace; crystal growth simulation

check for updates

Citation: Jeon, H.J.; Park, H.; Alhammadi, S.; Jung, J.H.; Kim, W.K. Optimal Magnetic Graphite Heater Design for Impurity Control in Single-Crystal Si Grower Using Crystal Growth Simulation. *Processes* **2022**, *10*, 70. https://doi.org/10.3390/pr10010070

Academic Editors: Bor-Yih Yu and Ioannis Spanopoulos

Received: 29 November 2021
Accepted: 25 December 2021
Published: 30 December 2021

Publisher's Note: MDPI stays neutral with regard to jurisdictional claims in published maps and institutional affiliations.

Copyright: © 2021 by the authors. Licensee MDPI, Basel, Switzerland. This article is an open access article distributed under the terms and conditions of the Creative Commons Attribution (CC BY) license (https://creativecommons.org/licenses/by/4.0/).

1. Introduction

The majority of single-crystal Si ingots currently used in semiconductor devices and solar cells are fabricated by the Czochralski (Cz) method [1]. In the Cz process, single-crystal ingot growth is initiated by establishing contact between a single-crystal Si seed and a molten Si in a rotating quartz crucible, and further growth is achieved by slowly pulling the ingot from the Si melt, with rotation in the opposite direction to the crucible [2–6]. Optimization of the Cz process and optimal design of a Cz reactor for low-cost and high-quality ingot and wafer production has been pursued to maintain competitiveness in the industry. One of the improvements involves applying an external magnetic field to stabilize the interface between the crystal and molten Si. However, this process requires a high initial investment because additional installation of large and expensive magnetic equipment is required, separate to the Cz reactor [7].

Therefore, we designed a new graphite heater to produce high-quality single-crystal ingots in a low-cost and stable manner by realizing the internal magnetic field from the graphite heater itself. Internal side graphite heaters are typically divided into three or multiple blocks for industrial applications as the implementation of a single block is not feasible because of the high load.

Impurities such as oxygen affect the formation of defects within the crystal ingots and wafers. Thus, effective control of the oxygen content is essential for the fabrication of high-quality wafers. Oxygen diffuses into the Si melt during crystal growth owing to the ablation of a quartz crucible made of silica (SiO_2). The incoming oxygen during crystal growth is present in an interstitial state. Oxygen in single-crystal Si can cause various precipitation defects, and excessive oxygen precipitation reduces the wafer strength. Oxygen precipitation near the surface of the wafer may induce the breakdown of the oxide film and leakage of the P–N current. Furthermore, oxygen can cause light-induced degradation and thus reduce cell efficiency in the case of solar cell wafers. Therefore, proper

control of the oxygen concentration during the ingot and wafer fabrication processes can reduce process losses due to defects [8–10].

Herein, we applied a traveling magnetic field inside the graphite heater to control the oxygen concentration during single-crystal Si ingot growth. Numerous theoretical and experimental studies on the correlation between crystal growth and internal magnetic field have been conducted [11–15]. For the first time, Hirata and Hoshikawa reported successful oxygen concentration control in the Si crystal by applying an axially symmetric cusp magnetic field for the Cz Si crystal growth process [11]. Ding et al. demonstrated that the anticlockwise periodical flow was induced in the melt by cusp magnetic field and this helped to reduce the impurity in the crystal by three-dimensional unsteady simulations for the 300 mm Cz single-crystal Si growth process [12].

Results of previous simulation studies indicate that the temperature variation at the periphery of growing crystals can be effectively reduced by controlling the temperature distribution, interface shape, and oxygen inflow with relatively low power consumption [16–19].

In this study, we divided the internal side graphite heater into arbitrary design sections to simulate the fabrication of low-cost high-quality single-crystal Si ingots and wafers. Furthermore, we investigated variations in the current intensities at constant conditions by an arbitrary magnetic graphite heater (AMGH); in addition, we modified the crystal growth furnace to increase the process efficiency. We conducted numerical simulations on the control of the oxygen concentration using a crystal growth simulator (CGSim).

2. Methods

2.1. Process and Mathematical Modeling

The procedure for the Cz process is illustrated in Figure 1. The steps are as follows: melting, vacuum, dipping, necking, shouldering, body growth, and tailing. The total process takes approximately 70 h or more based on the dimensions of the silicon ingot, which, in our case, had a height of 1050 mm and diameter of 205 mm [20,21]. Crystal growth needs to be manually controlled by adjusting the pulling speed and temperature of the quartz crucible to continuously control the power delivered to the quartz crucible. In addition, failure in the continuous control of the diameter during the process results in crystal lattice defects and breakage, thus requiring a restart from the initial stage of the re-melting process. To prevent this, direct observation by the human eye and efficient process control are necessary. The Cz process is very complex, and the quality of the product ingot is determined by the accuracy of the process control [22] on several process parameters, such as the ratio of the crystal growth rate (V) and the temperature gradient (G) of the silicon in the melt–crystal interface (V/G), content of vacancies and interstitials, free defect area, von Mises stress (related to the destruction of the crystal), and influx of oxygen, one of the representative impurities [23–25]. To grow high-quality silicon ingots, certain variables must be considered to control the molten state to prevent oxygen injection into the crystal ingot while maintaining the quality of the defect-free area of the melt–crystal interface and crystal thermal stress [26–28].

Crystal growth simulation (CGSim) is simulation software for simulating the growth of single-crystal and polycrystalline materials from their melts. This enables the visualization of the process of heat flow and heat transfer inside the reactor by simulating the interaction of fluid and gas in engineering problems using a computer and obtaining an approximate solution. CGSim is applicable to heat transfer, fluid mechanics, and electromagnetics because it can simulate the flow of molten Si and extremely high-temperature processes and apply magnetic field effects. In actual engineering, data are collected, applied, and modeled and external factors, such as the required physical properties and loads, are set. Thus, the visualized results were derived for verification and optimization through simulation.

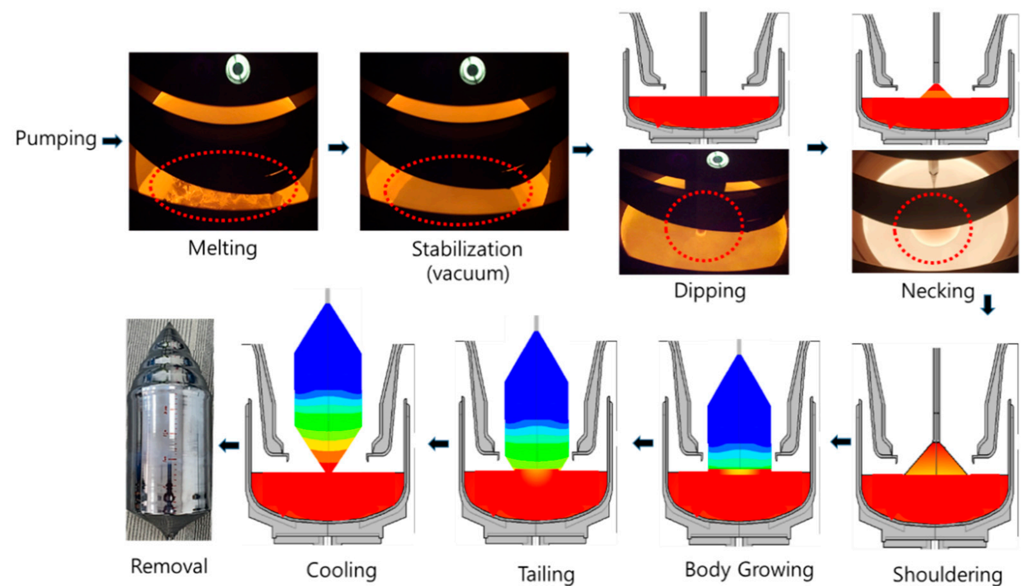

Figure 1. Cz process for single-crystal Si growing.

Therefore, CGSim was used to achieve the optimal design, process conditions, crystal quality improvement through heat transfer, temperature analysis, gas and melt convection analyses, and calculation of the crystal defects and stresses. The shape of the Cz grower is axially symmetric, but the essence of the growing crystal is isotropic. Therefore, in the growing process, the coincidence with the central axis of the triple point is very complicated, and it is difficult to achieve perfect symmetry. Therefore, this study assumed axisymmetry using rotation to reduce asymmetric patterns. The Cz growth simulation used a two-dimensional cylindrical coordinate system [26]. In the Cz process, research has been performed on computational models of dimensionless numbers such as Reynolds (Re), Grashof (Gr), Prandtl (Pr), Marangoni (Ma), Rayleigh (Ra), and Peclet (Pe) numbers [25]. To analyze the temperature distribution and fluid flow in the Cz process, the continuity equation,

$$\frac{\partial \rho}{\partial t} + \nabla \cdot (\rho \mathrm{u}) = 0, \tag{1}$$

momentum equation of each velocity component,

$$\rho \frac{Du}{Dt} = -\nabla p + \nabla \cdot \tau + \rho g, \tag{2}$$

and energy equation,

$$\rho \frac{\partial e}{\partial t} + p(\nabla \cdot u) = \nabla(\mathrm{k} \nabla \mathrm{T}) + \varphi, \tag{3}$$

are applied, assuming an incompressible fluid and expressed in Cartesian coordinates in the form of a tensor. In the equations, $\frac{D}{Dt}$, ρ, u, ∇, p, and t are the convective derivative, density, velocity, divergence, pressure, and time, respectively. τ represents the second-order deviatoric stress tensor, g is the gravitational acceleration applied to the continuum, φ is a viscous dissipation function, and k represents the thermal conductivity. In the case of dimensionless numbers, the crystallization rate of Si in this study corresponds to the heat flux, transition, and melting of the crystal, which is expressed as [28]:

$$\rho_{\mathrm{crystal}} \Delta \mathrm{H} \mathrm{u}_{\mathrm{n}} = \left(\lambda \frac{\mathrm{dT}}{\mathrm{dn}}\right)_{\mathrm{melt}} - \left(\lambda \frac{\mathrm{dT}}{\mathrm{dn}}\right)_{\mathrm{crystal}} \tag{4}$$

where $\mathrm{u_n}$ is the average rate of partial crystallization at the melt–crystal interface; ΔH is the crystallization calorific value (crystallization calories), which is also called the heat of

crystallization, 1.8×10^6 J/kg; and $\rho_{crystal}$ is the thermal conductivity of solid Si at the melting point, 66.5 W/mK.

The average crystallization rate υ is calculated by fluidly integrating the vertical crystallization rate u_v in space S with the partial crystallization rate u_n at the solid–liquid interface, as follows:

$$\upsilon = \frac{1}{s}\int u_v ds \quad (5)$$

The flow due to surface tension occurs in a high-temperature region with a small surface tension toward a low-temperature region. In other words, flow occurs in the direction of the interface in the wall of the quartz crucible. Accordingly, there is a synergistic effect in the direction of flow owing to the difference between the density, flow of the fluid, and surface tension. The total flow occurs from the crucible to the interface of the surface portion and from the interface to the lower center of the surface. The rotation of the crucible and crystal mainly produces a circumferential flow, and the dimensionless number that can show the effect of this rotation is the rotational Re. The speed and specific length of the crystal and crucible are denoted by Ω_x, Ω_c, and L, respectively, and the rotational Re is defined as

$$\mathcal{R}e_x = \frac{\Omega_x L^2}{v} \quad (6)$$

$$\mathcal{R}e_c = \frac{\Omega_c L^2}{v} \quad (7)$$

Here, the form of the forced convection flow varies with Re but that of the natural convection flow changes with changes in Gr, which represents the ratio of the buoyant force acting on the fluid to the viscous force.

The Pr number represents the contribution of the momentum diffusion rate to the thermal diffusion rate of laminar flow, $C_p\mu/k$. The Ra of a fluid is a dimensionless number for buoyancy-driven flow, also known as free convection or natural convection [29–31], which characterizes the fluid flow system. Certain lower range values indicate laminar flow, and higher range values indicate turbulence. Below a certain threshold, the absence of fluid motion indicates that heat is transferred by conduction rather than convection. Ra is defined as the product of Gr, representing the relationship between the buoyancy force and viscosity of a fluid with a specific length x, and Pr, representing the relationship between the momentum diffusion and heat diffusion rates [32,33]:

$$\text{Ra} = \frac{g\beta\Delta T x^3}{v\alpha} = \frac{Time\ scale\ for\ thermal\ transport\ via\ diffusion}{time\ scale\ for\ thermal\ transport\ via\ convection\ at\ speed\ u} \quad (8)$$

When there is a difference in the surface tension, a flow occurs. The Cz process, in which pure materials are grown, expresses the surface tension as a function of temperature. Therefore, a temperature difference can drive the flow, which is called thermal capillary motion. Ma is a dimensionless parameter that represents the amount of the flow due to surface tension. If σ is the surface tension of the liquid phase, L is the thickness of the fluid and α is the heat diffusion. then Ma is expressed as [34]

$$\text{Ma} = -\left(\frac{\partial\sigma}{\partial T}\right)\frac{L\Delta T}{\alpha v}. \quad (9)$$

Pe describes the transport phenomenon of a continuum and defines the rate of diffusion of the same amount driven by an appropriate temperature gradient as the ratio of the heat transfer rate of a physical quantity by convection. Analysis of the liquid heat-resistant transfer mechanism is necessary, and when the average velocity in the system is U_0, this number is expressed as [34]

$$Pe_T = \frac{U_0 L}{\alpha}. \quad (10)$$

The software used for the simulation was CGSim® of the STR Group (St. Petersburg, Russia), which can analyze and optimize crystal growth processes, including conventional Cz, liquid-encapsulated Cz, vapor pressure-controlled Cz, and Bridgman growth. The CGSim (melt) software can simulate the process of single-crystal ingot growth from the melt of crystals and produces different results depending on the internal structure, crystal size, and shape of the quartz crucible.

The simulation was performed considering the quality determination of the Si crystal growth according to the design of an AMGH to decrease the impurity concentration. Table 1 lists the key material properties, such as thermal performance and emissivity, where Ar and carbon felt were used as an inert gas and an insulating material, respectively. The cooling system affects the temperature gradient inside the crystal during the growth process. Conductive graphite was used as a magnetic field heater [35–37].

Table 1. Properties of materials related to the Cz process [38].

Materials	Properties	Value
Si crystal	Heat capacity (J/kg)	1000
	Heat conductivity(W/m)	75.22
	Emissivity	0.7
Si melt	Heat capacity (J/kg)	915
	Heat conductivity(W/m)	66.5
	Emissivity	0.3
	Density (kg/m^3)	$3194 - 0.3701 \times T(K)$
	Melting temperature (K)	1685
	Latent heat (J/kg)	1.8×10^6
	Wetting angle (degree)	11
	Surface tension (N/m)	0.7835
	Dynamic viscosity (Pa·s)	0.0008
	Marangoni coefficient (N/(m·K))	0.0001
Graphite	Heat capacity (J/kg)	720
	Heat conductivity(W/m)	105.26
	Emissivity	0.8
Quartz(crucible)	Heat capacity (J/kg)	1232
	Heat conductivity(W/m)	4
	Emissivity	0.85
Steel	Heat capacity (J/kg)	438
	Heat conductivity(W/m)	15
	Emissivity	0.45
Carbon felt	Heat conductivity(W/m)	0.02
	Emissivity	0.9
Ar	Heat capacity (J/kg)	521
	Heat conductivity(W/m)	3.06

2.2. Motivation of Impurities

The number of impurities introduced during the growth of a single-crystal Si ingot was determined by the segregation coefficient at the melt–crystal interface. For a low concentration of impurities, the solidification rate is slow and the segregation coefficient factor is very close to the equilibrium value. When the single-crystal Si ingot grows at a high growth rate, the inflow behavior of the dopant (dopant $k_0 < 1$) provides different results for different k in equilibrium. Therefore, it was determined that the value of k is proportional to the crystal growth rate of single-crystal Si ingots [39,40]. The reason for this behavior is that as the crystal growth rate increases, there is insufficient time for the impurity concentration to change near the interface to reach equilibrium with a constant diffusion coefficient. If the impurity concentration is very high near the interface, more impurities than expected can be introduced. Therefore, the effective segregation coefficient k_{eff} at this time is larger

than the value of k_0(ex., k_0(oxygen) = 1 in CGSim), in the equilibrium state. The effective segregation coefficient is expressed by the equation of Burton, Prim, and Schlichter:

$$k_{eff} = \frac{k_0}{k_0 + (1 - k_0)\exp(-\xi f/D)} \tag{11}$$

Here, k_0 is the separation factor in the equilibrium state of impurities, ξ is the thickness of the diffusion boundary layer, D is the diffusion coefficient of the impurity(ex., $D_O(cm^2/s) = 0.13 \times \exp(-2.53/k_B T)$ for oxygen [41]), and f is the growth rate. The thickness of the diffusion boundary layer was analyzed using the diffusion coefficient of impurities as

$$\xi = 1.6D^{1/3}\nu^{1/6}w^{-1/2}, \tag{12}$$

where ν is the viscosity of the melt, and w is the rotation rate of the crystal. In this expression, the inclusion rate is determined by the growth rate under the assumption that the other variables are constant at a given time. If the crystal growth rate is varied, the distribution of impurities is predicted to be non-uniform. In contrast, if the interface is horizontal and the thickness of the boundary layer is constant, a uniform distribution of impurities in the radial direction can be obtained [42–44].

Suppression and minimization of oxygen atoms that affect the characteristics of semiconductor devices and solar cells are important factors in the Cz crystal growth process. In this process, the ultra-high temperature is maintained while the single-crystal Si ingot grows. Figure 2 shows a quartz crucible composed of silica containing oxygen, which is utilized to melt polycrystalline Si lumps in the Cz process owing to its high melting temperature (~1700 °C), excellent heat resistance, and refractory nature. The Cz process requires a temperature of approximately 1414 °C (Si melting point) or higher. At extremely high temperatures, silica can be decomposed to oxygen, as in Equation (13), and then oxygen can diffuse into the Si melt, as shown in Figure 3.

$$SiO_2(s) = Si(l) + O_2 \tag{13}$$

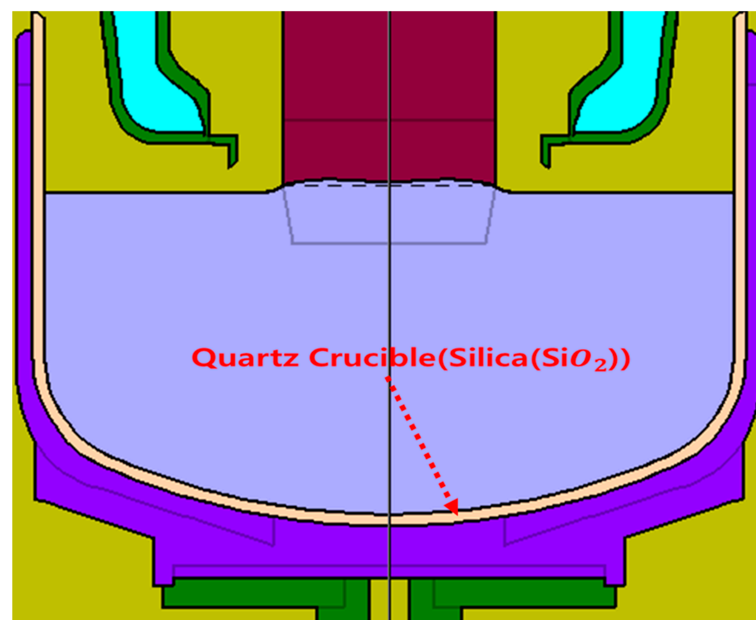

Figure 2. Quartz crucible composed of silica-containing oxygen.

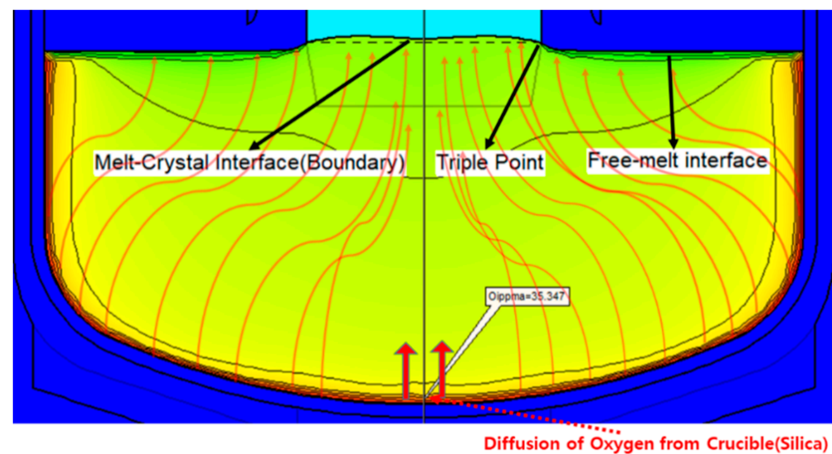

Figure 3. Oxygen inflow from the quartz crucible to crystal.

Most of the oxygen dissolved in the quartz crucible evaporated to the surface (free surface) of the molten *Si*. The amount of oxygen generated increased with the temperature. As the single-crystal *Si* ingot has a high cooling rate after crystal growth, it does not have an equilibrium condition with oxygen introduced into the crystal and thus exists in a supersaturated state. During the cooling process, some oxygen diffused to the outside, but most of the oxygen existed inside the crystal. The oxygen present in the crystal at room temperature is referred to as the initial oxygen concentration, which is the cause of oxygen precipitation in the subsequent heat treatment process of the single-crystal *Si* ingot.

Proper control of the oxygen concentration is necessary for the production of high-purity single-crystal Si ingots and wafers because oxygen is one of the primary crystal defects in the wafer. An excess concentration of oxygen is reported as 10^{18} atoms/cm^3. In the Cz process, metal impurities are controlled to less than 10^{12} atoms/cm^3, and the concentration of impurities added to the dopant is approximately 10^{14} atoms/cm^3, which is very low compared to the oxygen concentration. Therefore, most of the precipitates generated during the heat treatment process are assumed to be oxygen, and relevant studies to minimize the oxygen concentration have progressed remarkably [45–47].

3. Results and Discussion

In this study, a simulation was performed to reduce the concentration of oxygen, a representative impurity in the Cz process. The optimal structure inside the reactor was designed to overcome the limited conditions in a given process related to impurity control. It is known that oxygen produced in the quartz crucible (silica) is introduced into the crystal through the flow of high-purity molten Si fluid. It has been reported that the oxygen concentration can be controlled by controlling the pulling speed, rotation speed, and melt charge level [48]; however, to derive a high crystal growth rate, the rotation speed is required at a certain minimum value of rpm. To overcome these problems and maintain competitiveness in the global market, the design of the Cz process for low-cost and high-quality ingots should be achieved. As shown in Figure 4, a possible approach is to apply an external magnetic field to the interface of the crystal and molten Si. However, applying a magnetic field requires a high initial investment cost because large and expensive electromagnetic equipment is installed outside the chamber. The normal Cz process controls convection by using magnetic devices installed outside the chamber to control the molten Si state [49–53]. As shown in Figure 5, the graphite heater that generates heat inside the Cz furnace is a coil-type MGH for impurity control. The optimal result was derived by utilizing the improved design of the Cz reactor and crystal growth simulation analysis. The designed MGH can control the fluid flow pattern inside the furnace according to the direction of the Lorentz force formed by the magnetic field. To verify the reduction of impurities, various MGHs were designed, and a comparative analysis was conducted.

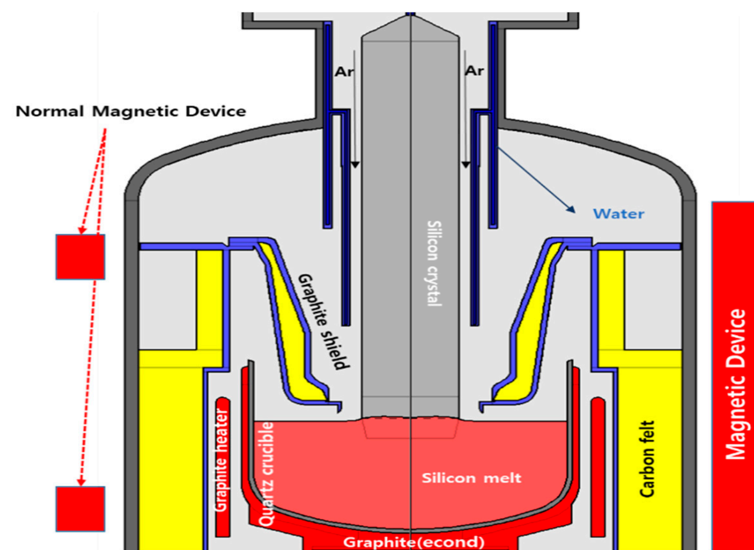

Figure 4. Applied magnetic field in normal Cz reactor.

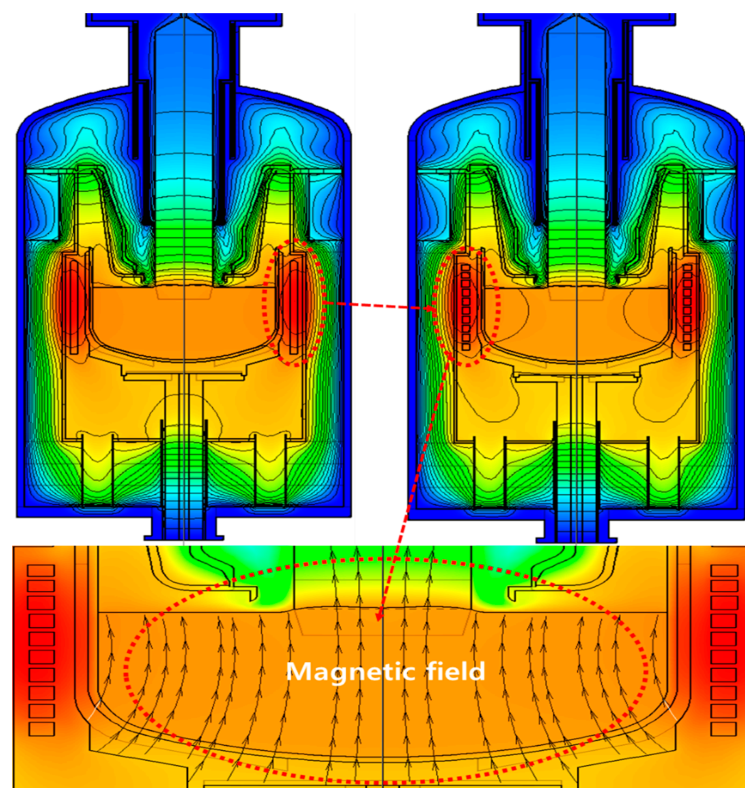

Figure 5. Proposed design of the magnetic graphite heater (MGH) in the Cz reactor.

A normal graphite heater (NGH) and an arbitrary magnetic field heater were analyzed. Unlike general heaters, magnetic field heaters are designed in the form of coils. Here, the electric field (E), magnetic field (B), vector field, and pseudo vector according to the time and position are represented as

$$\nabla \times H = J + \frac{\partial D}{\partial T} = J_s + J_e + J_V + \frac{\partial D}{\partial T}, \tag{14}$$

$$\nabla \times E = -\frac{\partial B}{\partial T},$$

$$\nabla \cdot B = 0,$$

$$\nabla \cdot D = \rho,$$

where ρ is the total charge density (total charge per unit volume), J is the total current density (total current per unit area), and D is the displacement field.

In addition, the Lorentz force generated along with the magnetic field was expressed as

$$FL = qE + qvB \quad (15)$$

Here, F_L is the Lorentz force applied to the particle, q is the charge of the particle (C), E is the electric field (V/m), v is the particle velocity (m/s), and B is the magnetic field (T). When the electric field E = 0, it can be inferred using this equation that the motion of the charged particles in the magnetic field is circular [54,55].

As shown in Figure 6, the direction of the magnetic field and the Lorentz force were determined according to the direction of the current, and a direct current (DC) was applied in this simulation. In the case of alternating current (AC), owing to the frequency, the flow of the fluid was difficult to control consistently, and thus, the formation of the vortex was not satisfactory. The DC results were more reliable, and thus, the DC MGH was applied as well.

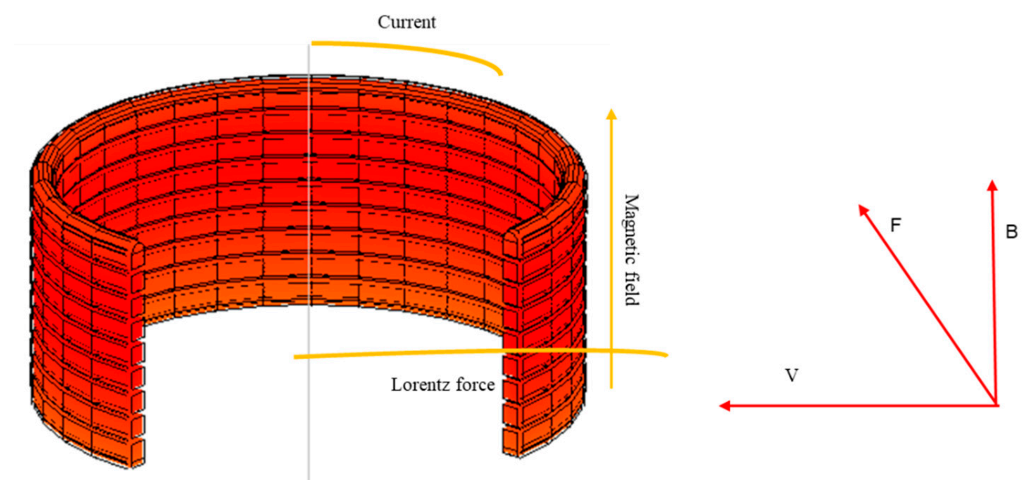

Figure 6. Direction of the magnetic field and Lorentz force according to the current.

The NGH was designed with a length of 400 mm and thickness of 30 mm. We confirmed the formation of a magnetic field and calculated its strength by dividing each heater into parts. Arbitrary MGHs were designed by dividing each heater into parts, and the formation of a magnetic field and its strength were compared for an equal applied DC current. At equal sizes and lengths, the results of a vortex phenomenon for different numbers of parts per coil was studied. As shown in Figure 7, the MGHs were of four structural designs: Arbitrary 3 Part MGH (A3MGH), 4 Part MGH (A4MGH), 5 Part MGH (A5MGH), and Poly MGH (APMGH).

Figure 8 shows the direction of the magnetic field and Lorentz force for each MGH design with the application of DC+ current, where the magnetic field was vertically formed from bottom to top, while the Lorentz force was nearly horizontally produced as expected by Equation (15).

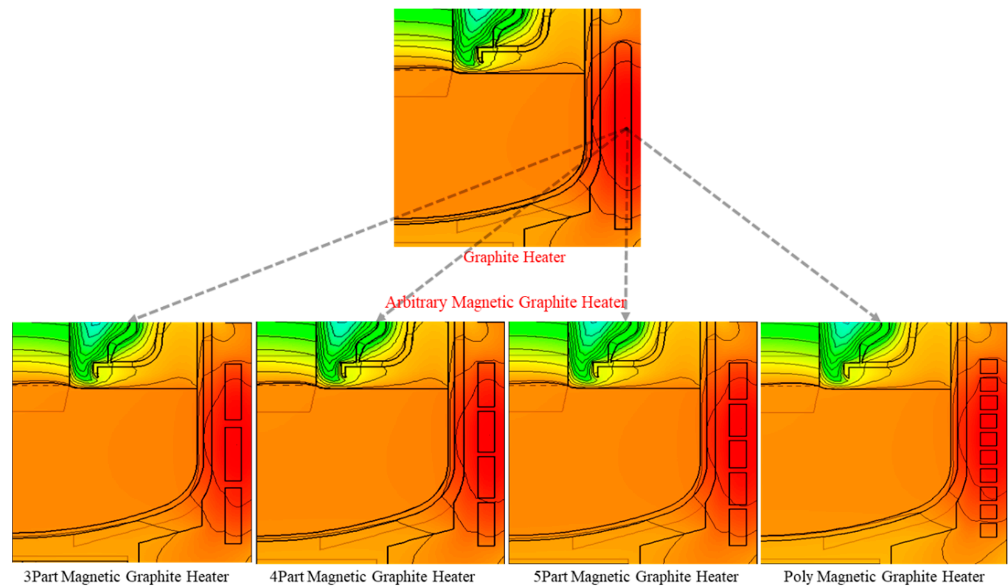

Figure 7. Design of A3MGH, A4MGH, A5MGH, and APMGH with different number of parts.

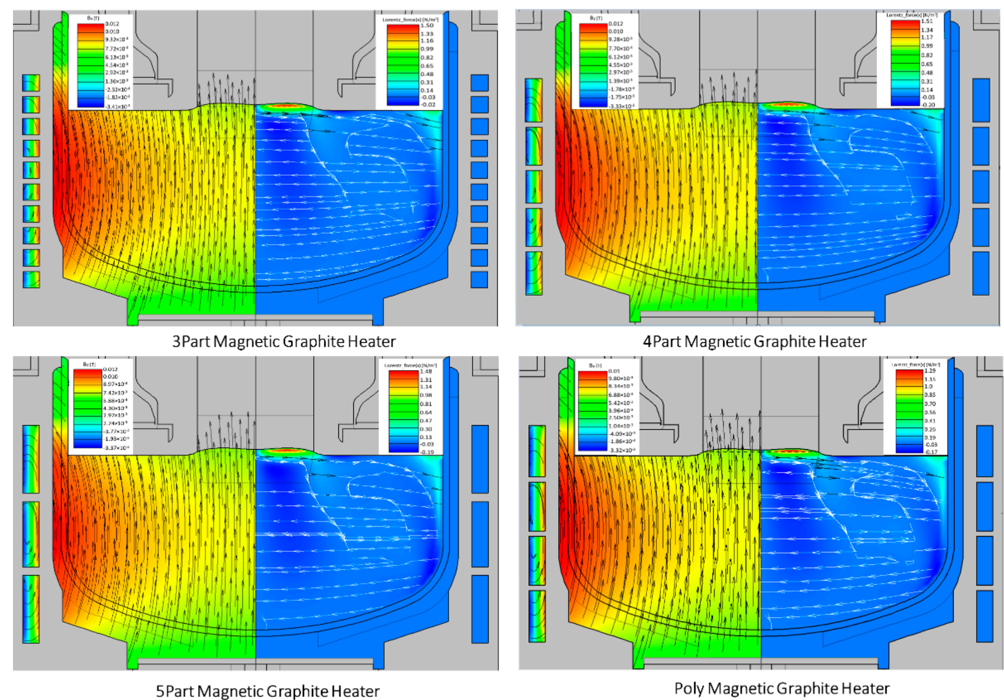

Figure 8. Direction of the magnetic field (**left**) and Lorentz force (**right**) and strength according to each design.

The corresponding intensities are compared in Figure 9. Although the four types of MGHs were set to an identical DC+ current of 6000 A, the strength of the magnetic field was different for each design. The strengths of the magnetic field and Lorentz force for different MGHs were estimated at the distance from the MGH to the center point of the crucible (i.e., center of the single-crystal Si ingot or Si melt) based on the surface of the molten Si and the solid-liquid interface.

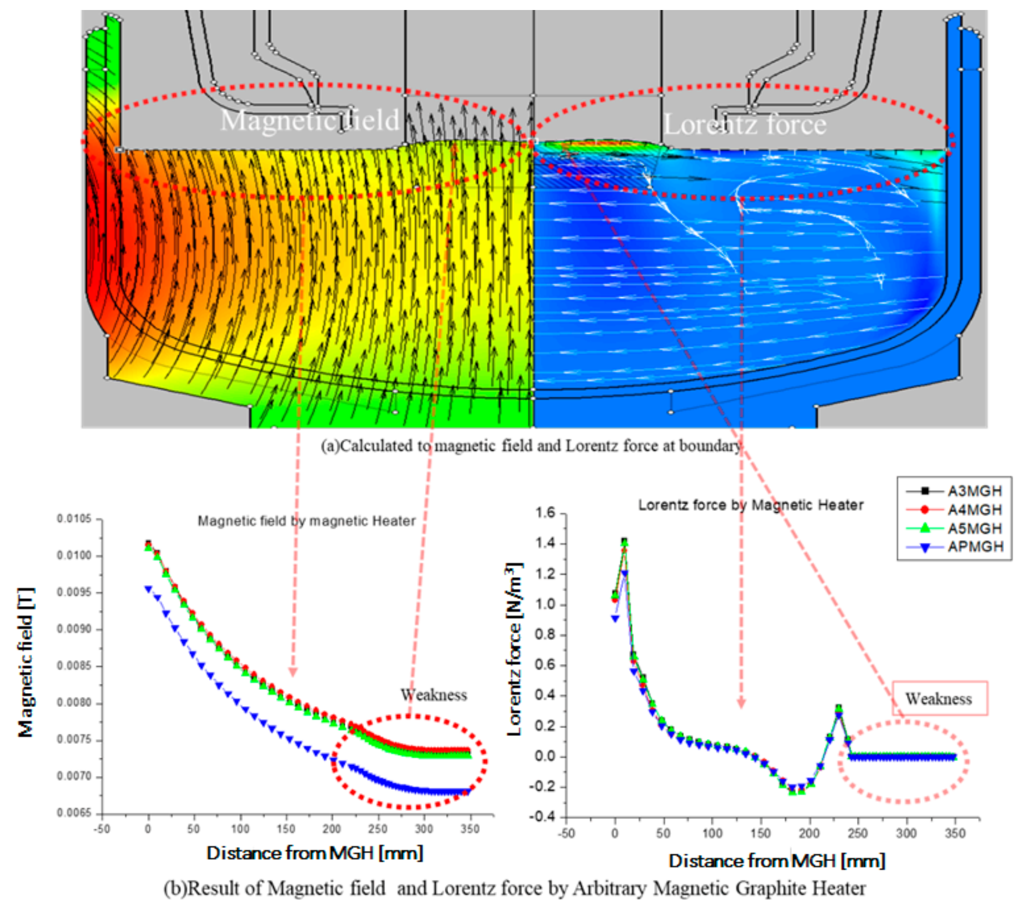

Figure 9. (**a**) Direction and (**b**) intensities of magnetic field and Lorentz force calculated from the interface.

Overall, the magnetic field strength decreased exponentially from the MGH to the center of the crucible. The Lorentz force strength also showed a similar trend, except for partial fluctuations. In the region close to the center of the crucible or Si melt, the magnetic field and Lorentz force strengths remained nearly unchanged. However, as shown in Figure 9b, among the four designs of A3MGH, A4MGH, A5MGH, and APMGH, the strength of the magnetic field of APMGH was substantially lower than those of the other three designs, which can affect the flow pattern of the fluid and thus the incorporation of oxygen into the growing ingot. Thus, the optimal MGH (OMGH) was determined by analyzing the oxygen concentration for each MGH.

Prior to comparing the oxygen concentration of the conventional NGH and the new MGH designs, the convection behavior of the molten Si inside the quartz crucible was investigated in terms of vortex and turbulent viscosity, as shown in Figure 10. It was confirmed that the NGH and MGHs showed significantly different convection patterns for vortices and slight differences in turbulent viscosity. Three large circular vortex flows were characterized in the Si melt affected by NGH. However, the design with MGHs showed that the circular vortices in the middle of the three vortex flows were merged into two other circular vortex flows at the wall and center of the crucible.

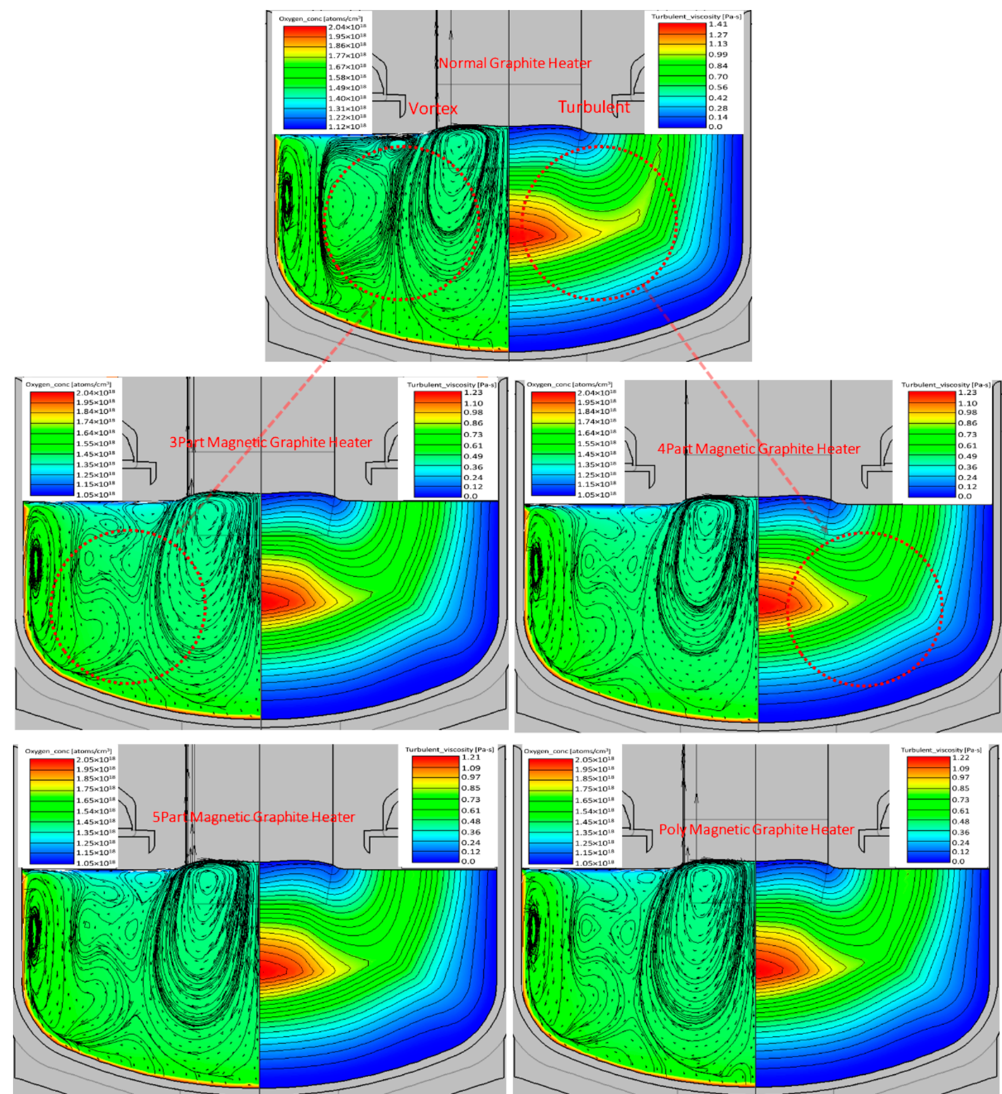

Figure 10. Convection of fluid and turbulent viscosity distribution by design.

The turbulent viscosity profiles with angles for NGH and MGHs are compared in Figure 11, where the turbulent viscosity for NGH was larger than that for MGHs over the entire angle. The APMGH design demonstrated the lowest turbulent viscosity, indicating the most stable flow. The simulation results suggest that the change in the flow pattern and the formation of vortices by heater design may affect the directionality of the oxygen present in the molten Si. Based on this, the free defect region (V/G) and von Mises stress considered for the growth of high-purity single-crystal Si ingots were analyzed. Furthermore, additional analyses focused on the reduction of the oxygen concentration.

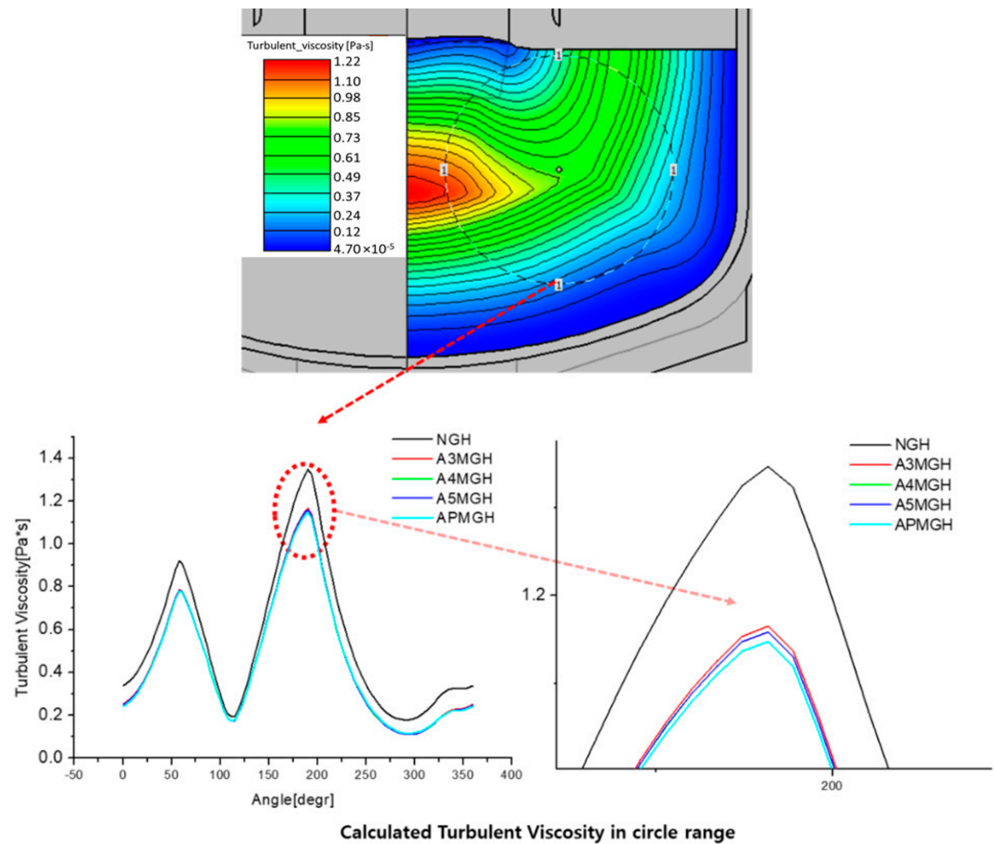

Figure 11. Comparison of turbulent viscosities in Si molten state by design.

In Figures 12 and 13, the values of V/G and the von Mises stress, which numerically represent the free defect region, were compared for different heater designs. Both results suggest that there is no significant difference between different graphite heater designs (e.g., a difference of less than 1%). In other words, it was confirmed that the magnetic field of the MGHs did not considerably influence the defect area and stress inside the crystal.

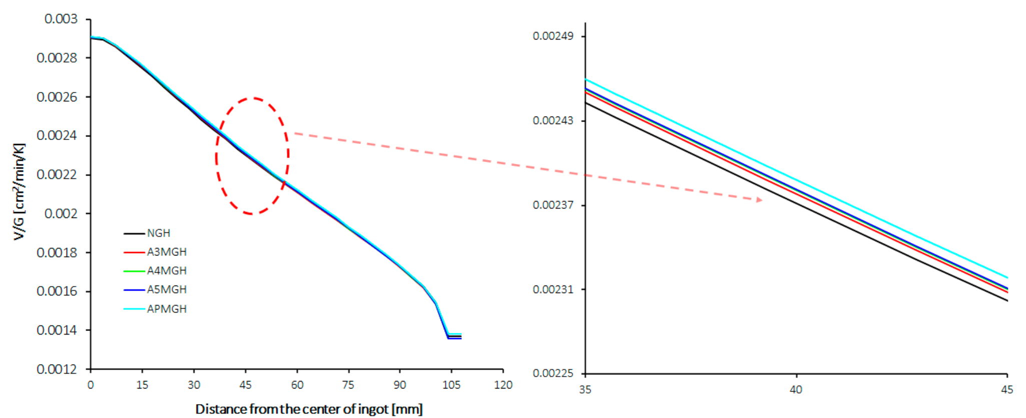

Figure 12. V/G results for each arbitrary graphite heater.

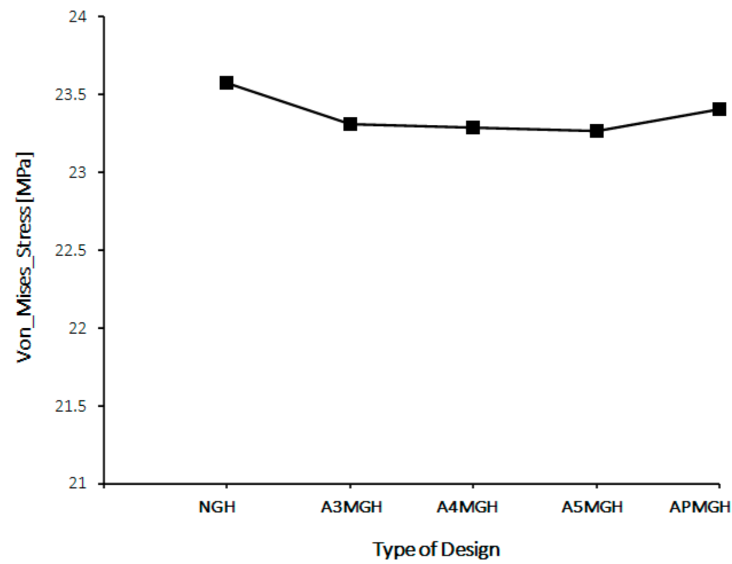

Figure 13. von Mises stress results for each arbitrary graphite heater.

Additionally, the total power consumption and applied DC+ current to achieve crystal growth are compared in Figure 14 and Table 2. Basic NGH showed the highest power consumption, which subsequently decreased as the number of parts in the MGH increased. The results confirmed that the amount of power consumed during the crystal growth process could be reduced by applying a DC current to the MGH. It should be noted that APMGH required the lowest power consumption and applied DC+ current.

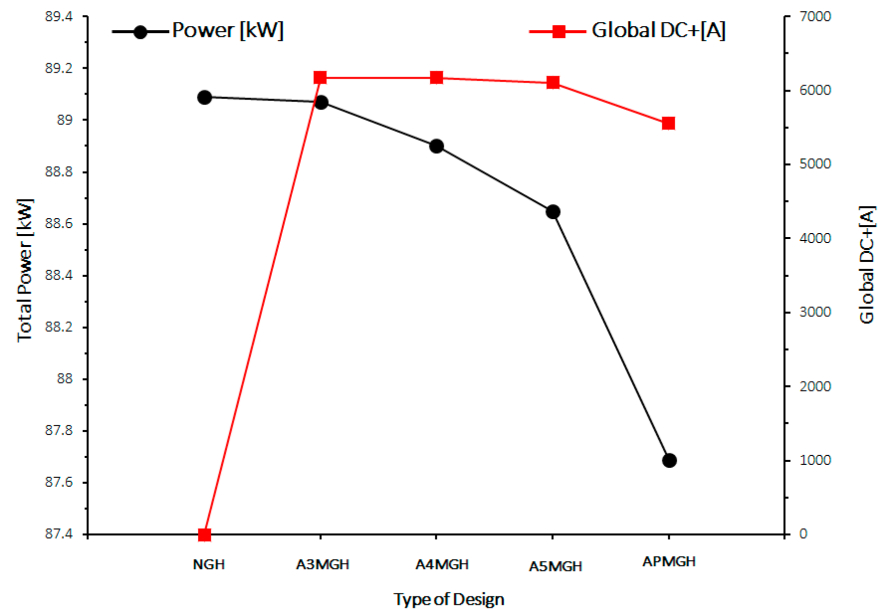

Figure 14. Power consumption and DC+ currents for each arbitrary graphite heater.

Table 2. CGSim power consumption and DC+ current analysis results for various graphite heaters.

	NGH	A3MGH	A4MGH	A5MGH	APMGH
Total Power [kW]	89.09	89.07	88.90	88.65	87.69
Global DC+[A]	0	6176.81	6170.72	6104.15	5556.09

Based on these results, a comparative analysis of the conventional graphite heater and AMGH with modified designs was conducted to determine the optimum MGH for reducing the oxygen concentration in the Si melt–crystal interface. Figure 15 shows the profiles of oxygen concentration at the Si melt–crystal interface for NGH and AMGHs, revealing that the AMGHs with a magnetic field resulted in a lower oxygen concentration than conventional NGH by approximately 4.8%. Among the four AMGHs, APMGH demonstrated a slightly lower oxygen concentration than the other three AMGHs. Therefore, it can be deduced that the concentration of oxygen flowing into the crystal can be reduced by stabilizing the melt–crystal interface using a magnetic field.

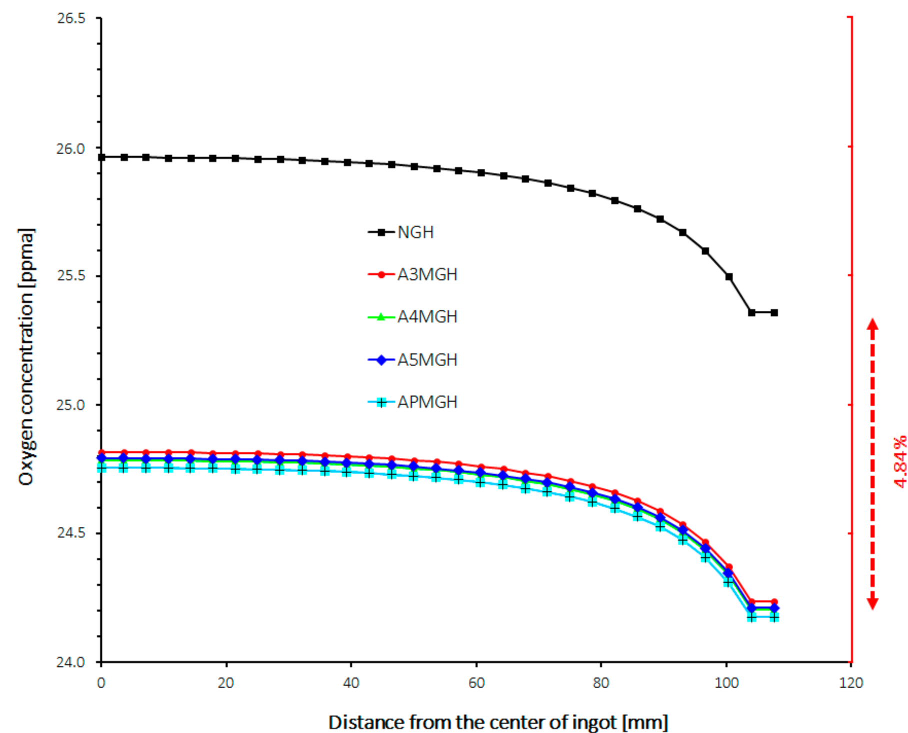

Figure 15. Analysis results of oxygen concentration at the melt–crystal interface.

4. Conclusions

This paper reported the CGSim simulation results for the process design of a Cz furnace to control impurities in single-crystal Si ingots. Under the given process conditions, it was demonstrated that replacing the NGH inside the chamber with coil-type AMGHs caused a vortex to form in the molten Si to suppress the inflow of oxygen. In addition, the AMGHs could affect the direction of oxygen diffusion and thus reduce the average oxygen concentration at the Si melt–crystal interface and power consumption by 4.8 and 10%, respectively, compared with the basic NGH. It is expected that the impurities can be further controlled by adjusting the process parameters, including the seed/crucible rotation and melt filling level. Further optimization of these processes is necessary for cost-effective commercialization in terms of lifetime enhancement and minimization of inherent defects.

Author Contributions: Conceptualization, H.J.J. and J.H.J.; methodology, H.J.J.; validation, J.H.J. and H.P., software and simulation, H.J.J.; formal analysis and evaluation, H.P. and H.J.J.; investigation, H.J.J., S.A. and H.P.; writing—original draft preparation, H.J.J. and S.A.; writing—review and editing, W.K.K.; visualization, H.J.J. and H.P.; supervision, J.H.J. and W.K.K.; project administration, J.H.J. and W.K.K.; funding acquisition, W.K.K. All authors have read and agreed to the published version of the manuscript.

Funding: This research was funded by the Korea Institute of Energy Technology Evaluation and Planning (KETEP) and the Ministry of Trade, Industry and Energy (MOTIE), Republic of Korea (grant number 20183010014320), and the Priority Research Centers Program through the National Research Foundation of Korea (NRF) funded by the Ministry of Education (grant number 2014R1A6A1031189).

Institutional Review Board Statement: Not applicable.

Informed Consent Statement: Not applicable.

Data Availability Statement: Not applicable.

Conflicts of Interest: The authors declare no conflict of interest.

Software: CGSim v.20 software (STR) was used in this study. Vladimir Artemyev from STR Group Inc. (http://str-soft.com, accessed on 1 November 2021) supported the software training.

References

1. Park, D.; Kim, M.; So, W.; Oh, S.-Y.; Park, H.; Jang, S.; Park, S.-H.; Kim, W.K. Evaluation of Bifacial Si Solar Module with Different Albedo Conditions. *Curr. Photovolt. Res.* **2018**, *6*, 62–67. [CrossRef]
2. Chen, Q.; Jiang, Y.; Yan, J.; Qin, M. Progress in modeling of fluid flows in crystal growth processes. *Prog. Nat. Sci.* **2008**, *18*, 1465–1473. [CrossRef]
3. Deai, H.; Iwasaki, T.; Ikematsu, Y.; Kawakami, K.; Harada, H.; Matsumura, A. Influence of crystal originated particles on gate oxide breakdown. *Jpn. J. Appl. Phys.* **1996**, *35*, 1476–1479. [CrossRef]
4. Friedrich, J.; von Ammon, W.; Müller, G. Czochralski growth of silicon crystals. In *Handbook of Crystal Growth*; Elsevier: Amsterdam, The Netherlands, 2014; pp. 45–104.
5. Wang, C.; Zhang, H.; Wang, T.; Ciszek, T. A continuous Czochralski silicon crystal growth system. *J. Cryst. Growth* **2003**, *250*, 209–214. [CrossRef]
6. Fisher, G.; Searist, M.R.; Standley, R.W. Silicon Crystal Growth and Wafer Technologies. *Proc. IEEE* **2012**, *100*, 1454–1474. [CrossRef]
7. Von Ammon, W.; Gelfgat, Y.; Gorbunov, L.; Muhlbauer, A.; Muiznieks, A.; Makarov, Y.; Virbulis, J.; Muller, G. Application of magnetic fields in industrial growth of silicon single crystals. In Proceedings of the Joint 15th Riga and 6th PAMIR International Conference on Fundamental and Applied MHD, Rigas, Latvia, 27 June–1 July 2005; pp. 41–45.
8. Kalaev, V.; Sattler, A.; Kadinski, L. Crystal twisting in Cz Si growth. *J. Cryst. Growth* **2015**, *413*, 12–16. [CrossRef]
9. Zhao, W.; Li, J.; Liu, L. Control of Oxygen Impurities in a Continuous-Feeding Czochralski-Silicon Crystal Growth by the Double-Crucible Method. *Crystals* **2021**, *11*, 264. [CrossRef]
10. Voronkov, V.-V.; Falster, R. Vacancy-type microdefect formation in Czochralski silicon. *J. Cryst. Growth* **1998**, *194*, 76–88. [CrossRef]
11. Hirata, H.; Hoshikawa, K. Silicon crystal growth in a cusp magnetic field. *J. Cryst. Growth* **1989**, *96*, 747–755. [CrossRef]
12. Ding, J.; Li, Y.; Liu, L. Effect of cusp magnetic field on the turbulent melt flow and crystal/melt interface during large-size Czochralski silicon crystal growth. *Int. J. Therm. Sci.* **2021**, *170*, 107137. [CrossRef]
13. Collet, Y.; Magotte, O.; Van den Bogaert, N.; Rolinsky, R.; Loix, F.; Jacot, M.; Regnier, V.; Marchal, J.-M.; Durpet, F. Effective simulation of the effect of a transverse magnetic field (TMF) in Czochralski Silicon growth. *J. Cryst. Growth* **2012**, *360*, 18–24. [CrossRef]
14. Frank-Rotsch, C.; Dropka, N.; Kießling, F.-M.; Rudolph, P. Semiconductor Crystal Growth under the Influence of Magnetic Fields. *Cryst. Res. Technol.* **2020**, *55*, 1900115. [CrossRef]
15. Kakimoto, K.; Eguchi, M.; Ozoe, H. Use of an inhomogenous magnetic field for silicon crystal growth. *J. Cryst. Growth* **1997**, *180*, 442–449. [CrossRef]
16. Huang, X.; Taishi, T.; Wang, T.; Hoshikawa, K. Measurement of temperature gradient in Czochralski silicon crystal growth. *J. Cryst. Growth* **2001**, *229*, 6–10. [CrossRef]
17. Nam, W.; Hahn, Y.; Baik, S. Local optimization of graphite heater to save a power consumption of Czochralski Si ingot grower for PV application. *Energy Procedia* **2017**, *124*, 767–776. [CrossRef]
18. Yokoyama, R.; Nakamura, T.; Sugimura, W.; Ono, T.; Fujiwara, T.; Kakimoto, K. Time-dependent behavior of melt flow in the industrial scale silicon Czochralski growth with a transverse magnetic field. *J. Cryst. Growth* **2001**, *519*, 77–83. [CrossRef]
19. Naguyen, T.H.T.; Chen, J.-J.; Hu, C.; Chen, C.-H. Numerical simulation of heat and mass transfer during Czochralski silicon crystal growth under the application of crystal-crucible counter- and iso-rotations. *J. Cryst. Growth* **2019**, *507*, 50–57. [CrossRef]
20. Seigneur, H.; Mohajeri, N.; Brooker, K.R.P.; Davis, O.; Schneller, E.J.; Dhere, N.G.; Rodgers, M.P.; Wohlgemuth, J.; Shiradkar, N.S.; Scardera, G.; et al. Manufacturing metrology for c-Si photovoltaic module reliability and durability, Part I: Feedstock, crystallization and wafering. *Renew. Sustain. Energy Rev.* **2016**, *59*, 84–106.
21. Gaspar, G.M.M.; Autruffe, A.; Pó, J.-M. Silicon growth technologies for PV applications. In *New Research on Silicon—Structure, Properties, Technology, Vitalyi Igorevich Talanin*; IntechOpen: London, UK, 2017. [CrossRef]
22. Phuc, L.T.H.; Jeon, H.; Truong, N.T.N.; Hak, J.J. Improving the Dipping Step in Czochraski Process Using Haar-Cascade Algorithm. *Electronics* **2019**, *8*, 646. [CrossRef]

23. Kalaev, V.; Lukanin, D.; Zabelin, V.; Makarov, Y.N.; Virbulis, J.; Dornberger, E.; Von Ammon, W. Calculation of bulk defects in CZ Si growth: Impact of melt turbulent fluctuations. *J. Cryst. Growth* **2003**, *250*, 203–208. [CrossRef]
24. Voronkov, V.; Falster, R. Vacancy and self-interstitial concentration incorporated into growing silicon crystals. *J. Appl. Phys.* **1999**, *86*, 5975–5982. [CrossRef]
25. Mukaiyama, Y.; Sueoka, K.; Maeda, S.; Iizuka, M.; Mamedov, V.M. Numerical analysis of effect of thermal stress depending on pulling rate on behavior of intrinsic point defects in large-diameter Si crystal grown by Czochralski method. *J. Cryst. Growth* **2020**, *531*, 125334. [CrossRef]
26. Sortland, Ø.-S.; Øvrelid, E.-J.; M'Hamdi, M.; Di Sabatino, M. Investigation of pinholes in Czochralski silicon ingots in relation to structure loss. *J. Cryst. Growth* **2019**, *510*, 1–6. [CrossRef]
27. Shockley, W.; Read, W., Jr. Statistics of the recombinations of holes and electrons. *Phys. Rev. Rev.* **1952**, *87*, 835–842. [CrossRef]
28. Forrest, E.C.; Hu, L.-W.; Buongiorno, J.; McKrell, T.J. Convective heat transfer in a high aspect ratio minichannel heated on one side. *J. Heat Transf.* **2016**, *138*, 021704. [CrossRef]
29. Evstratov, I.Y.; Alaev, V.V.; Zhmakin, A.I.; Makarov, Y.N.; Abramov, A.G.; Ivanov, N.G.; Smirnov, E.M.; Dornberger, E.; Virbulis, J.; Tomzig, E.; et al. Modeling analysis of unsteady three-dimensional turbulent melt flow during Czochralski growth of Si crystals. *J. Cryst. Growth* **2001**, *230*, 22–29. [CrossRef]
30. Patience, G.-S. *Experimental Methods and Instrumentation for Chemical Engineers*; Elsevier: Amsterdam, The Netherlands, 2013; pp. 227–263. [CrossRef]
31. Lord Rayleigh, O.M.F.R.S. LIX.On convection currents in a horizontal layer of fluid, when the higher temperature is on the under side. *Phil. Mag.* **2009**, *32*, 529–546. [CrossRef]
32. Çengel, Y.; Turner, R.; Cimbala, J. *Fundamentals of Thermal-Fluid Sciences*, 5th ed.; McGraw-Hill Education: New York, NY, USA, 2017; pp. 715–820.
33. Squires, M.-T.; Quake, S.-R. Microfluidics: Fluid physics at the nanoliter scale. *Rev. Mod. Phys.* **2005**, *77*, 977–1026. [CrossRef]
34. Patankar, S.-V. *Numerical Heat Transfer and Fluid Flow*; McGraw-Hill Education: New York, NY, USA, 1980; p. 715.
35. Prostomolotov, A.-I.; Verezub, N.-A.; Mezhennii, M.-V.; Reznik, V.-Y. Thermal optimization of CZ bulk growth and wafer annealing for crystalline dislocation-free silicon. *J. Cryst. Growth* **2011**, *318*, 187–192. [CrossRef]
36. Sim, B.-C.; Jung, Y.-H.; Lee, H.-W. Effect of the ingot cooling on the grown-in defects in silicon Czochralski growth. *Jpn. J. Appl. Phys.* **2009**, *48*, 105503. [CrossRef]
37. Zhao, W.; Liu, L. Control of heat transfer in continuous-feeding Czochralski-silicon crystal growth with a water-cooled jacket. *J. Cryst. Growth* **2017**, *458*, 31–36. [CrossRef]
38. Jeon, H.J.; Park, H.; Koyyada, G.; Alhammadi, S.; Jung, J.H. Optimal Cooling System Design for Increasing the Crystal Growth Rate of Single-Crystal Silicon Ingots in the Czochralski Process Using the Crystal Growth Simulation. *Processes* **2020**, *8*, 1077. [CrossRef]
39. Fumio, S. Single-Crystal Silicon: Growth and Properties. In *Springer Handbook of Electronic and Photonic Materials*; Springer: Cham, Switzerland, 2017. [CrossRef]
40. Digges, T.-G.; Shima, R. The Effect of Growth Rate, Diameter and Impurities Concentration on structure Czochralski silicon crystal growth. *J. Cryst. Growth* **1980**, *50*, 865–869. [CrossRef]
41. Kulkarni, M.S. Defect dynamics in the presence of oxygen in growing Czochralski silicon crystals. *J. Cryst. Growth* **2007**, *303*, 438–448. [CrossRef]
42. Hopkins, R.-H.; Seidensticker, R.-G.; Davis, J.-R.; Choudhruy, P.-R.; Blais, P.D. Crystal growth considerations in the use of solar grade silicon. *J. Cryst. Growth* **1997**, *42*, 493–498. [CrossRef]
43. Burton, J.-A.; Prim, R.-C.; Slichter, W.-P. The distribution of solute in crystals grown from the melt. Part I. Theoretical. *J. Chem. Phys.* **1953**, *21*, 1987–1991. [CrossRef]
44. Yen, C.-T.; Tiller, W.-A. Oxygen partitioning analysis during Czochralski silicon crystal growth via a dopant marker and a simple transfer function modeling techniqueII. Growth velocity and applied magnetic field transients. *J. Cryst. Growth* **1991**, *109*, 142–148. [CrossRef]
45. Huang, X.; Terashima, K.; Izunome, K.; Kimura, S. Effect of antimony-doping on the oxygen segregation coefficient in silicon crystal growth. *J. Cryst. Growth* **1995**, *149*, 59–63. [CrossRef]
46. Izunome, K.; Huang, X.; Togawa, S.; Terashima, K.; Kimura, S. Control of oxygen concentration in heavily antimony-doped Czochralski Si crystals by ambient argon pressure. *J. Cryst. Growth* **1995**, *151*, 291–294. [CrossRef]
47. Zhang, J.; Liu, D.; Zhao, Y.; Jiao, S. Impact of heat shield structure in the growth process of Czochralski silicon derived from numerical simulation. *Chin. J. Mech. Eng.* **2014**, *27*, 504–510. [CrossRef]
48. Jeon, H.-J.; Park, J.-H.; Artemyev, V.; Hwang, S.-H.; Song, S.-J.; Kim, N.-Y.; Jung, J.-H. A Czochralski process design for Si-Single crystal O_2 impurity minimization with pulling rate, rotation speed and melt charge level optimization. *Korean Chem. Eng. Res.* **2020**, *58*, 369–380. [CrossRef]
49. Hong, Y.-H.; Shim, K.-B. Effect of asymmetric magnetic fields on the interface shape in Czochralski silicon crystals. *J. Korean Cryst. Growth Cryst. Technol.* **2008**, *18*, 140–145.
50. Jana, S.; Dost, S.; Kumar, V.-V.; Durst, F. A numerical simulation study for the Czochralski growth process of Si under magnetic field. *Int. J. Eng. Sci.* **2006**, *44*, 554–573. [CrossRef]

51. Ivanov, N.-G.; Korsakov, A.-B.; Smirnov, E.M.; Khodosevitch, K.-V.; Kalaev, V.-V.; Makarov, Y.-N.; Dornberger, E.; Virbulis, J.; von Ammon, W. Analysis of magnetic field effect on 3D melt flow in CZ Si growth. *J. Cryst. Growth* **2003**, *250*, 183–188. [CrossRef]
52. Cen, X.-R.; Zhan, J.; Li, Y.-S. Large eddy simulation of Marangoni convection in Czochralski crystal growth. *Cryst. Res. Technol.* **2011**, *46*, 14–22. [CrossRef]
53. Grabner, O.; Muller, G.; Virbulis, J.; Tomzig, E.; von Ammon, W. Effects of various magnetic field configurations on temperature distributions in Czochralski silicon melts. *Microelectron. Eng.* **2001**, *56*, 83–88. [CrossRef]
54. Kivelson, M.; Russell, C.T. *Introduction to Space Physics*; Cambridge University Press: Cambridge, NY, USA, 1995; p. 29.
55. Dehel, T.-F.; Dickinson, M.; Lorge, F.; Startzel, R., Jr. Electric field and Lorentz force contribution to atmosphere vortex phenomena. *J. Electrostat.* **2007**, *65*, 631–638. [CrossRef]